Contents lists available at ScienceDirect

Transactions of Nonferrous Metals Society of China

36(2026) 68−79

www.tnmsc.cn

Precipitation behavior of *S′* phase in rapid cold punched Al−Cu−Mg alloy

Ze-yi HU [a,b], Pu-yu LI [a], Cai-he FAN [a,*], Shuai WU [a,**], Yi-ling LU [b], Yin-chun XIAO [a], Ling OU [a]

[a] College of Materials and Advanced-Manufacturing, Hunan University of Technology, Zhuzhou 412007, China;
[b] College of Science and Engineering, University of Derby, Derby, DE22 3BB, UK

Abstract: The evolution of the *S′* precipitate in Al−Cu−Mg alloy was investigated using transmission electron microscopy (TEM), high-angle annular dark-field scanning transmission electron microscopy (HAADF−STEM), molecular dynamics (MD) simulations, and other analytical techniques. The precipitation behavior during different aging stages of the supersaturated solid solution formed after rapid cold punching was focused, which induces rapid dissolution of precipitates. The findings reveal that the precipitation sequence is significantly influenced by aging temperature. At higher aging temperatures, which mitigate lattice distortion in the matrix, the precipitation sequence follows the conventional path. Conversely, at lower aging temperatures, where lattice distortion persists, the sequence deviates, suppressing the formation of Guinier−Preston−Bagaryatsky (GPB) zones. MD simulations confirm that the variations in solute atom diffusion rates at different aging temperatures lead to the differences in the *S′* phase precipitation sequence.

Keywords: Al−Cu−Mg alloy; aging treatment; *S′* phase evolution; rapid cold punching; molecular dynamics simulations

1 Introduction

Al−Cu−Mg alloys are widely utilized in industries such as aerospace, weaponry, and rail transportation due to their high specific strength, excellent heat resistance, and superior formability [1−4]. The strengthening mechanisms primarily include deformation strengthening and precipitation strengthening. Thermomechanical treatment, which integrates both approaches, not only enhances work hardening but also alleviates deformation-induced stress [5−7]. This process facilitates the dispersion, nucleation, and growth of precipitate phases, potentially altering their characteristics and precipitation sequence [8−10].

WANG et al [11] conducted stress-relaxation aging experiments and finite element simulations to investigate the stress-relaxation behavior of aluminum alloys. Their experimental results demonstrated that pre-deformation not only enhances the strength of the samples but also accelerates the aging precipitation process, thereby reducing the time required to reach peak strength. Cold rolling led to variations in the aspect ratios of *S* phase (Al_2CuMg) precipitates during both growth and coarsening stages. IRMER et al [12] studied the effect of cold rolling on the precipitation behavior of Al−Cu−Mg alloys and found that clusters were disrupted during cold rolling and did not reconstitute during natural aging. Solute atoms appeared to be trapped in vacancy-solute clusters by forest dislocations, making them unavailable for the formation of clusters or Guinier−Preston−Bagaryatsky (GPB) zones. HUANG et al [13] employed three-dimensional atom probe, differential

Corresponding author: *Cai-he FAN, Tel: +86-731-22183466, E-mail: Fancaihe@hut.edu.cn;
**Shuai WU, Tel: +86-731-22183464, E-mail: 1094664267@qq.com
https://doi.org/10.1016/S1003-6326(25)66949-4
Received 22 October 2024; accepted 16 June 2025

thermal analysis, and transmission electron microscopy (TEM) to examine the redissolution of precipitated phase in Al−Cu alloys during plastic deformation and the subsequent reprecipitation behavior during aging. Their findings revealed a significantly accelerated precipitation rate of the θ phase (Al_2Cu) following redissolution during the aging process. Moreover, the precipitation sequence deviated from the conventional order, bypassing the transition phases, θ'' and θ', and directly transitioning from the Guinier−Preston (GP) zones to the equilibrium phase θ.

LI et al [14] concluded that the type of precipitates in re-aged samples after cold rolling was influenced by the re-aging temperatures and durations. The precipitated phases mainly consisted of GPB zones at lower temperatures or shorter time, whereas the S' phase was formed at higher temperatures and longer time. The dislocation density decreased with increasing re-aging temperatures and durations, and a recovery process, rather than recrystallization, occurred during re-aging. ZHANG et al [15] investigated the influence of multidirectional compression deformation on the precipitates of Al−Cu alloys and observed that severe plastic deformation led to the redissolution of the precipitates, resulting in a supersaturated solid solution. During the aging process, the precipitation rate was significantly accelerated. The precipitation sequence was determined by the heating temperature, the extent of deformation, and the post-deformation grain size, all of which were closely related to the precipitation behavior. HU et al [16] found that long plate-shaped S' phase underwent significant distortion, brittle fracture, separation, and redissolution during rapid cold punching deformation. Upon aging, reprecipitation occurred, and the morphology of the aging precipitates was characterized mainly by long flakes and granules. Several studies have indicated that pre-deformation increases the concentration of crystalline defects (particularly dislocations) and alters the distribution of secondary phase particles, thereby affecting their coherency, shape, dimensions, aspect ratio, interparticle spacing, volume fraction, and number density. These changes contribute to the enhanced strength of Al−Cu−Mg alloys during aging [2,17−20].

Typically, the strength of the alloy is primarily derived from nanoscale precipitates formed through natural or artificial aging following solution treatment and quenching [14,21−23]. Therefore, understanding the microstructure evolution of Al−Cu−Mg alloys during heat treatment, particularly the characteristics of aging precipitation phases, such as their type, size, distribution, and volume fraction, is crucial for achieving high performance. However, while considerable research has been conducted on the mechanisms of θ phase breakage, redissolution, and subsequent aging precipitation in Al−Cu alloys during severe plastic deformation, there is limited discussion on the reprecipitation behavior of the S' phase in Al−Cu−Mg alloys during aging following dissolution caused by severe plastic deformation. This study aims to provide insights into the heat treatment process for producing high-strength and resilient Al−Cu−Mg alloys. Additionally, it seeks to establish a theoretical foundation for understanding the aging and reprecipitation behavior of precipitates resulting from rapid cold-punching deformation.

2 Experimental

The fine-grained Al−Cu−Mg alloy cylindrical billet was rapidly solidified through spray forming using a self-developed SD380 large-scale spray-forming apparatus. The chemical composition of the alloy was determined using an optical emission spectrometer (OES) and is presented in Table 1. Subsequently, the cylindrical billet was extruded into a d30 mm round bar using a 1250 t extruder at an extrusion temperature of 450 °C and an extrusion ratio of 15∶1. The round bar was then cut into d30 mm × 20 mm cylindrical samples using a wire-cutting machine. The extruded specimens were subjected to rapid cold punching through 4 passes at 25 °C using a self-designed punching mold. A schematic representation of the rapid cold punching process is illustrated in Fig. 1. Following this, the samples were artificially aged at temperatures of 160, 180, and 200 °C for durations ranging from 0.2 to 30 h. After aging, the samples were air-cooled to room temperature. The detailed process parameters for rapid cold punching are summarized in Table 2.

For microstructural examination and hardness testing, samples were extracted from artificially aged specimens that had undergone rapid cold

Table 1 Chemical composition of Al−Cu−Mg alloy (wt.%)

Cu	Mg	Mn	Si	Fe	Al
4.51	1.46	0.56	<0.05	<0.05	Bal.

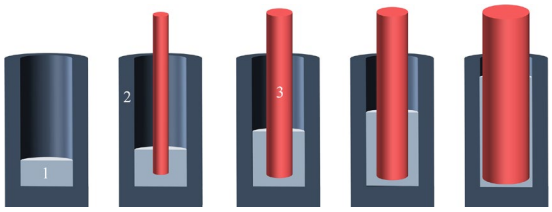

Fig. 1 Schematic of rapid cold punching: 1−Sample; 2−Drawing die; 3−Punch

Table 2 Process parameters of rapid cold punching

Punch	Diameter/mm	Velocity/(mm·s^{-1})
One-pass	10	30
Two-pass	14	25
Three-pass	20	20
Four-pass	27	15

punching. A JEM−F200 transmission electron microscope (TEM) was utilized to analyze the morphology, size, and distribution of the nanoprecipitate phases within the samples. The TEM samples were mechanically pre-thinned to a thickness of approximately 80 μm and subsequently subjected to electrolytic double-jet thinning using a nitric acid−methanol electrolyte (volume ratio of 1∶3) at a temperature below −25 °C. High-angle annular dark field scanning transmission electron microscopy (HAADF−STEM) was employed for sample observation under the following conditions: an accelerating voltage of 200 keV, an electron beam half-convergence angle of 10 mrad, a high-angle annular probe collection internal half-angle of 36 mrad, and a beam spot diameter of 0.20 nm. The dislocation density of the samples in different states was determined by measuring the lengths of dislocations in 150 TEM images captured at the same magnification. All TEM images were aligned along the $[001]_{Al}$ direction. Vickers micro-hardness measurements were performed using a pyramid diamond indenter to monitor the evolution of aging hardening. A load of 100 g was applied for 10 s and each sample was measured at a minimum of 15 points, with the measurement locations situated in the central region of the outer surface of the cylinder wall.

The molecular dynamics simulation was conducted using the LAMMPS (Large-scale Atomic/Molecular Massively Parallel Simulator) software. The initial dimensions of the aluminum system in the *X*, *Y*, and *Z* directions were set to be 4 nm each. The size of the precipitate was defined as 20 Å × 9 Å × 9 Å. A cavity matching the size of the precipitate was created in the center of the aluminum matrix, and the precipitate was subsequently inserted into this location. The system was then expanded threefold in the *X* and *Y* directions and fivefold in the *Z* direction to form the final simulation system, as illustrated in Fig. 2. In this study, the embedded atom method (EAM) potential was employed to describe the interactions between different atoms.

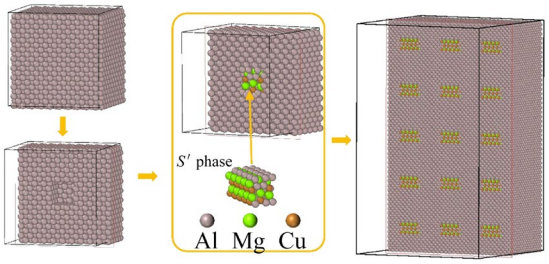

Fig. 2 Simulation system construction diagram

To optimize computational efficiency, a region with a diameter of 3 nm at the top of the *Z* direction was designated as a rigid body, enabling movement in the negative *Z* direction to simulate the cold punching process. The downward movement speed was set to be 0.1 Å/ps. Following the cold punching simulation, the system was heated from 300 K to the target temperature at a rate of 1 K/ps under isothermal-isobaric (NPT) conditions. Upon reaching the target temperature, the system was maintained for 100 ps to observe atomic diffusion. Although the holding time in the simulation is significantly shorter than in actual experimental conditions, the atomic motion trajectories can still be effectively observed and compared with the actual situation [24].

3 Results

3.1 Aging hardening curves

Figure 3 illustrates the hardness variation of samples aged at different temperatures over durations ranging 0.2−30 h. The age-hardening curves exhibited similar trends across all temperatures.

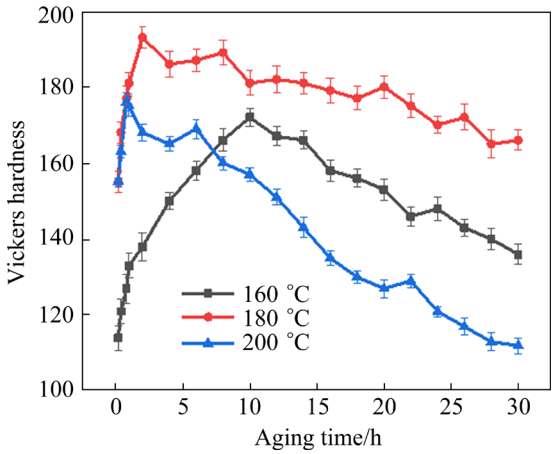

Fig. 3 Hardness curve of samples at different aging temperatures

Initially, the hardness increased rapidly during the early stages of aging, followed by a significant decline after reaching peak hardness. Higher aging temperatures significantly reduced the aging response time. For example, at 200 °C, the aging response time decreased from 10 h (for the peak-aged sample at 160 °C) to only 0.8 h. Additionally, at 180 °C, the sample achieved its maximum peak hardness of HV 193 within a short aging response time of 2 h.

3.2 TEM observation

3.2.1 Aging precipitation behavior at 160 °C

Figure 4 presents the TEM and high-resolution TEM (HRTEM) images of samples aged at 160 °C for 0.5, 2, 10, and 20 h. In the sample aged for 0.5 h, a significant number of dislocation lines were observed, some of which exhibited curling and intertwining. However, no precipitated phase was detected in this state (Figs. 4(a, e)). The sample aged for 2 h displayed dislocations along with a small amount of the S' phase (Fig. 4(b)). The HRTEM image of the S' phase revealed a thickness of approximately 1 nm (Fig. 4(f)). At the peak aging duration of 10 h, the dislocation density decreased significantly, while the abundance of the S' phase increased (Fig. 4(c)). In this state, the thickness of the S' phase was approximately 5 nm (Fig. 4(g)). After 20 h of aging, the dislocation density further decreased, accompanied by a reduction in the presence of the S' phase (Fig. 4(d)). Compared to the sample aged for 10 h, the thickness of the S' phase slightly increased, reaching approximately 7 nm (Fig. 4(h)).

3.2.2 Aging precipitation behavior at 180 °C

Figure 5 presents the characterization of rapid cold-punched samples aged at 180 °C for 0.5 h and 1 h, revealing the microstructural evolution during aging. The S' phase in the Al alloy is identified by diffraction spots, as shown in Figs. 5(a, c). After 0.5 h of aging, a discernible amount of the S' phase was observed, accompanied by curling dislocations distributed around the phases (Fig. 5(a)). The thickness of the S' phase at this stage was approximately 2 nm (Fig. 5(b)). After aging for 1 h, a noticeable increase in the number of S' phases was

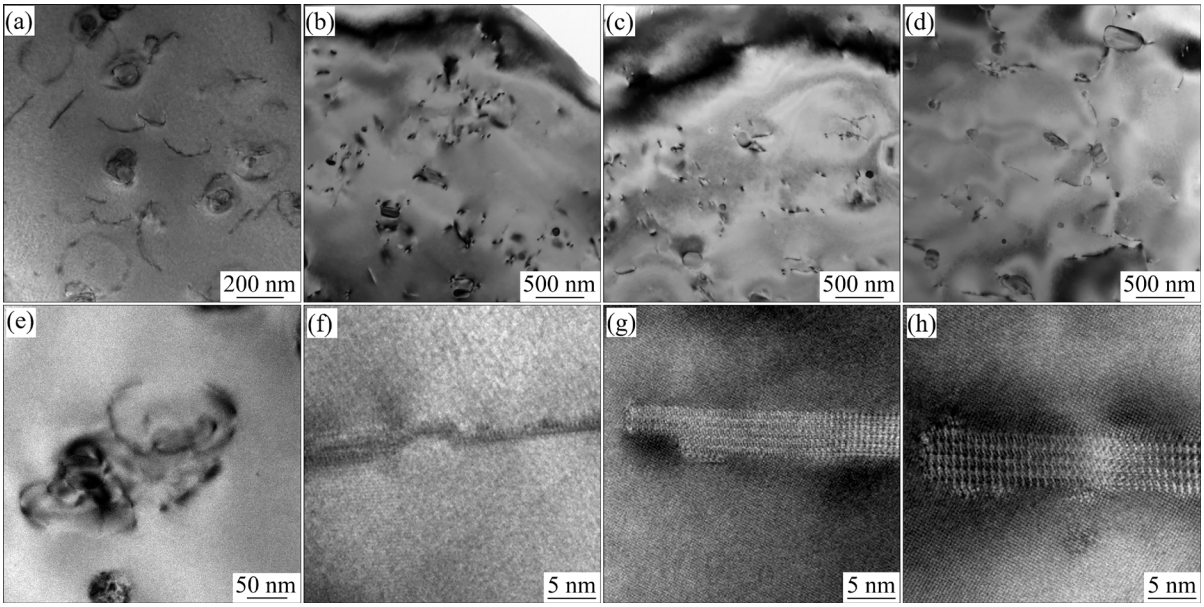

Fig. 4 TEM (a−d) and HRTEM (e−h) images of samples aged at 160 °C for 0.5 h (a, e), 2 h (b, f), 10 h (c, g) and 20 h (d, h)

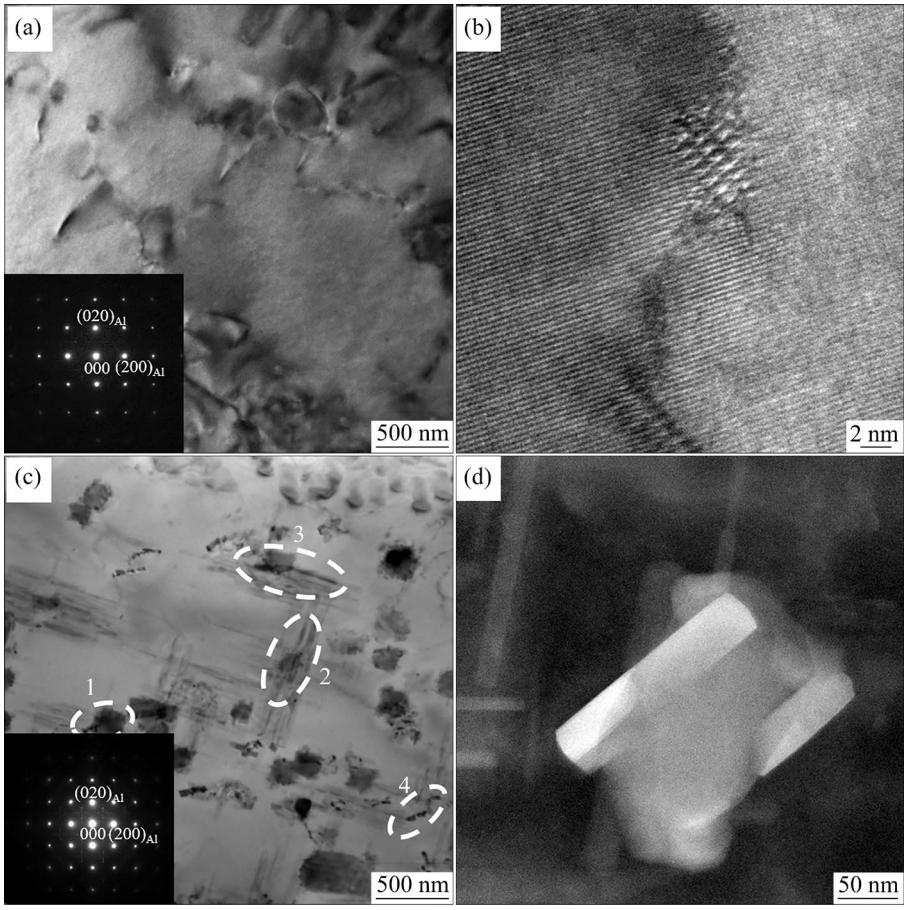

Fig. 5 TEM (a, c), HRTEM (b) and HAADF−STEM (d) images of samples aged at 180 ℃ for 0.5 h (a, b) and 1 h (c, d) (The insets in (a) and (c) are SAED patterns)

observed compared to the sample aged for 0.5 h, as illustrated in Fig. 5(c). The precipitation morphology of the *S′* phase on the *T* phase ($Al_{20}Cu_2Mn_3$) is labeled as No. 1, while Nos. 2 and 3 denote two mutually perpendicular morphologies. The *S′* phase exhibits a parallel orientation, with its $[001]_{S'}$ direction aligned with the matrix $[100]_{Al}$ and $[010]_{Al}$. Number 4 highlights the precipitation morphology of the *S′* phase at the dislocation. Additionally, the *S′* phase precipitated into the *T* phase, as depicted in Fig. 5(d). Notably, the *T* phase can capture dislocations, and since the *S′* phase generally prefers nucleation on dislocations, the interface between the *T* phase and the aluminum matrix becomes a favorable site for *S′* phase nucleation [25−27]. This explains the dense distribution of the *S′* phase around the *T* phase.

Figure 6 presents the characterization of precipitates in a sample aged at 180 ℃ for 2 h, corresponding to the peak-aged condition. Compared to the underaged sample, there was a significant increase in the number of *S′* phases at this stage, accompanied by a more uniform distribution. Furthermore, numerous needle-like precipitates were observed in the gaps among the *S′* phases (Fig. 6(a)). The corresponding diffraction spots in Fig. 6(b) confirm that these needle-like precipitates correspond to the GPB zones. The thickness of the *S′* phase at this stage was 5 nm approximately or greater (Fig. 6(c)). Figure 6(d) illustrates a uniform distribution of the GPB zones within the aluminum matrix. To further analyze the morphological characteristics of the GPB zones, the HAADF−STEM imaging was employed. HAADF−STEM is highly sensitive to heavy atoms, enabling clearer observations of structural characteristics such as morphology and size. In this case, the contrast of the GPB zones, which are richer in Cu atoms than in Al and Mg atoms, appears brighter than that of the matrix. Statistical measurements indicate that the average size of the GPB zones is approximately 2 nm (Fig. 6(e)). The structural unit of the GPB zone in this experimental alloy is consistent with that reported in the

literature [28]. It consists of a series of one-dimensional needles composed of $Mg_{(2x+2)}Cu_{(2x+2)}Al_{(3x+2)}$. Figure 6(e) displays two adjacent GPB structural units, with the Cu atomic column spacing (G) being twice that of the $(010)_{Al}$ plane spacing. A three-dimensional structural diagram of the GPB unit is shown in Fig. 6(f).

Figure 7 presents TEM and HRTEM images of the sample aged at 180 °C for 10 h, corresponding to the overaged state. Compared to the peak-aged sample (Fig. 6(a)), the distribution of the S' phase in this sample is uneven, exhibiting both dense and sparse regions (Fig. 7(a)). Notably, a significant precipitation-free zone is observed near the grain boundaries (Fig. 7(b)). The thickness of the S' phase in the overaged state increased compared to that in the sample aged at 180 °C for 2 h (Fig. 6(c)), reaching approximately 10 nm (Fig. 7(c)). However, no GPB zones were observed at this stage. The absence of GPB zones may be attributed to the transformation of most GPB zones into the S' phase during the overaging process.

3.2.3 Aging precipitation behavior at 200 ℃

Figure 8 shows TEM, HAADF−STEM, and HRTEM images of samples aged at 200 ℃ for 0.5 h and 0.8 h, offering valuable insights into the

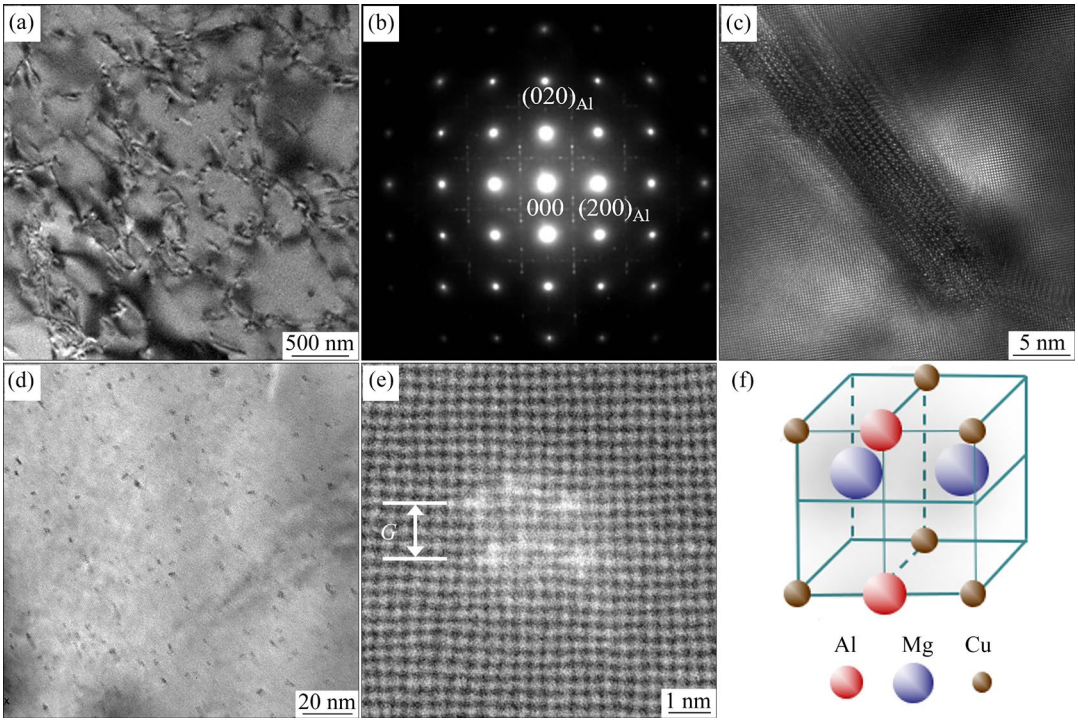

Fig. 6 TEM images of sample aged at 180 °C for 2 h: (a) TEM image of S' phase; (b) $[001]_{Al}$ SAED pattern; (c) HRTEM image of S' phase; (d) TEM image of GPB zones; (e) HAADF−STEM image of GPB zones; (f) 3D model of GPB structural unit

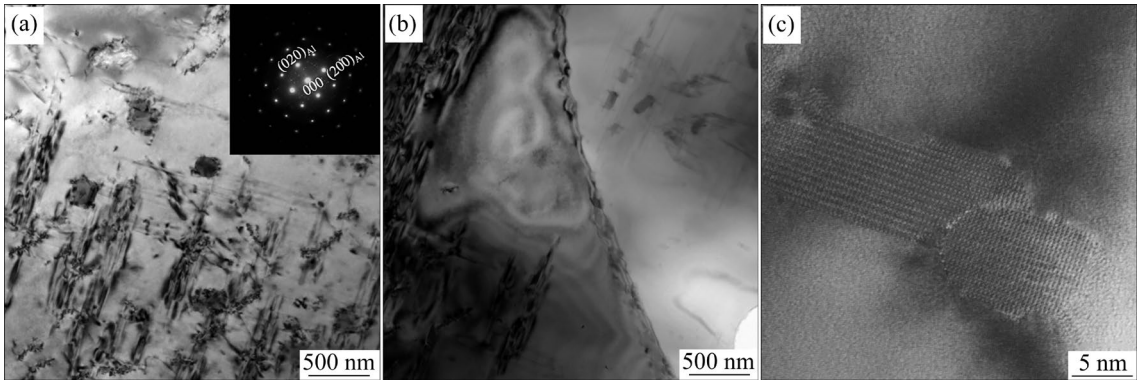

Fig. 7 TEM (a, b) and HRTEM (c) images of sample aged at 180 ℃ for 10 h, viewed along $[001]_{Al}$ direction

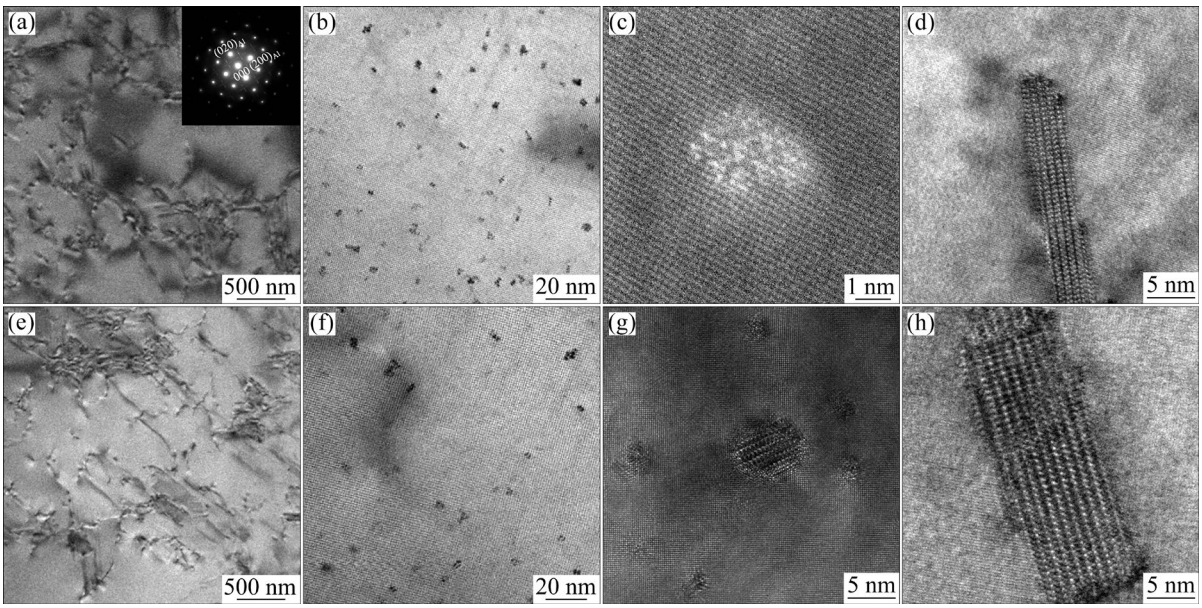

Fig. 8 TEM (a, b, e, f), HAADF−STEM (c) and HRTEM (d, g, h) images of samples aged at 200 ℃ for 0.5 h (a−d) and 0.8 h (e−h)

microstructural evolution at these elevated aging temperatures. In the sample aged for 0.5 h, a significant number of *S′* phases and GPB zones were observed, with dislocations surrounding the precipitated phases (Fig. 8(a)). The GPB zones were uniformly distributed, with an average size of approximately 3 nm (Figs. 8(b, c)). Furthermore, the thickness of the *S′* phase in this sample was approximately 4 nm (Fig. 8(d)). Upon aging for 0.8 h, corresponding to the peak aging state at this temperature, the dislocation density decreased significantly. The number of *S′* phases increased compared to the previous stage (Fig. 8(e)). However, the quantity of GPB zones decreased substantially, while their sizes increased (Fig. 8(f)). In HRTEM mode, a portion of the GPB zones transformed into small *S′* phases (Fig. 8(g)). Additionally, the *S′* phase exhibited visible coarsening at this stage, with a thickness of approximately 10 nm (Fig. 8(h)).

Figure 9 presents TEM and HRTEM images of samples aged at 200 °C for 2 h and 10 h. In the sample aged for 2 h (Figs. 9(a, b)), a significant reduction in the number of *S′* phases was observed compared to the previous stage. Concurrently, as the thickness of the *S′* phase increased, the curling dislocations noted in earlier stages disappeared indicating the transformation and coarsening of the *S′* phase during the aging process. After aging for 10 h, a broader grain-boundary precipitation-free zone became evident (Fig. 9(c)). This zone was wider than the precipitation-free zone observed in the sample aged for 10 h at 180 °C (Fig. 7(b)). At this stage, the *S′* phase exhibited noticeable coarsening, with a thickness of approximately 18 nm (Fig. 9(d)).

4 Discussion

Based on previous research findings [16], it is established that during the rapid cold punching process, the long plate-shaped *S′* phase in the extruded Al−Cu−Mg alloy undergoes significant distortion, brittle fracture, separation, and redissolution. This results in the transformation of the long plate-shaped *S′* phase into short rods or even complete redissolution and disappearance, causing the matrix to become a supersaturated solid solution. Consequently, the concentration of solute atoms within the aluminum matrix increases. The rise in strain and surface energy due to the fracture of precipitate particles leads to an increase in the free energy of the precipitate phases. Additionally, the enhanced interfacial distortion energy and stored strain energy during cold deformation contribute to a significant increase in the free energy of the system. According to the study by XU [29], if the aging temperature is insufficient to

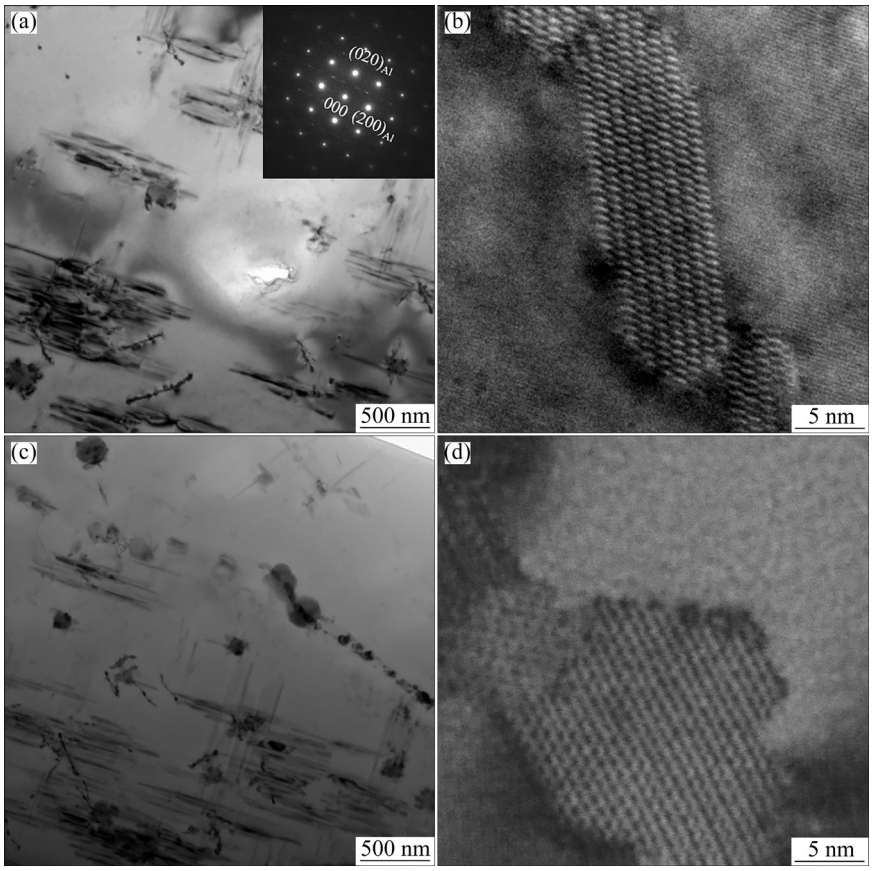

Fig. 9 TEM (a, c) and HRTEM (b, d) images of samples aged at 200 ℃ for 2 h (a, b) and 10 h (c, d)

eliminate lattice distortion in the matrix during the aging process, it becomes challenging to precipitate a transition phase that maintains a semi-coherent relationship with the matrix. This semi-coherent relationship further elevates the strain energy within the matrix, resulting in higher free energy and hindering the precipitation process.

In this experiment, no formation of GPB zones was observed during the low-temperature aging process at 160 °C. This phenomenon may be attributed to the higher free energy of the system, which suppresses the formation of GPB zones. Instead, the *S*′ phase precipitated directly, contributing to the reduction of the free energy of the system and achieving the energy balance. During the high-temperature aging process at 200 °C, the temperature was sufficient to eliminate lattice distortion in the matrix, leading to the traditional sequential precipitation of GPB zones → *S*′ phase. In the aging process at 180 °C, a small amount of the *S*′ phase initially precipitated, followed by the formation of GPB zones and continued precipitation of the *S*′ phase. In the initial stage of aging, the higher free energy of the system promoted the initial precipitation of the *S*′ phase to reduce the free energy of the system. Once the free energy of the system reached the equilibrium, precipitation followed the traditional sequence.

Furthermore, the coexistence of multiple phases is frequently observed in the experiment, and the presence of GPB zones (an unstable phase) is not limited to the early stages of aging. Even in peak-aged samples at 180 and 200 °C, GPB zones can still be detected. Therefore, it can be inferred that the precipitation process of the *S*′ phase does not strictly follow a linear progression with aging time. The nucleation and growth of the *S*′ phase may occur at any time before reaching the peak aging stage.

In addition, the rapid cold punching process before aging is conducted at low temperatures, high strains, and high strain rates, while solid-state diffusion primarily relies on the thermal activation of atoms, which is only achievable at higher temperatures. As a result, the diffusion process of solute atoms is limited, and the diffusion distance is short. Most of the Cu and Mg atoms remain clustered around the *S*′ phase prior to redissolution.

When the deformation ceases, a small portion of the S' phase remains incompletely dissolved. During the aging process, these incompletely dissolved S' phases serve as nucleation sites, promoting the uphill diffusion of surrounding solute atoms.

The essence of the aging process lies in the nucleation and growth of precipitate phases, which primarily depend on the diffusion of solute atoms. The relationship between the diffusion coefficient (D) and aging temperature can be expressed as follows [30]:

$$D = D_0 \exp\left(\frac{-Q}{RT}\right) \tag{1}$$

where D_0 represents the diffusion constant, Q denotes the activation energy, R is the molar gas constant, and T corresponds to the aging temperature. According to Eq. (1), the diffusion coefficient increases with rising aging temperature. As the aging temperature increases, the diffusion rate of solute atoms accelerates, leading to a shorter time required to reach peak aging conditions. Figure 3 illustrates that at 160 °C, the rapid cold-punched sample reached peak aging after 10 h, whereas at 200 °C, it only took 0.8 h to reach peak aging.

Furthermore, the nucleation rate (N) of the precipitated phase is also influenced by the aging temperature, as described by the following expression [31]:

$$N = C\left[\exp\left(\frac{-\Delta G^*}{KT}\right)\exp\left(\frac{-Q}{RT}\right)\right] \tag{2}$$

where C represents a constant, ΔG^* denotes the nucleation barrier, and K is the Boltzmann constant. According to Eq. (2), the nucleation rate of the precipitate phases increases with temperature. Figures 4 and 6 demonstrate that the quantity of precipitate phases in the sample aged at 180 °C for 2 h is significantly greater than that in the sample aged at 160 °C for 2 h, as a higher aging temperature enhances the nucleation rates of both the GPB zones and the S' phase.

However, according to Ref. [32], excessively high aging temperatures can reduce the formation of precipitate phases and the supersaturation of solute atoms within the matrix. This increases the nucleation barrier required for precipitate formation, resulting in a lower nucleation rate of precipitate phases. Figure 9 demonstrates that at an aging temperature of 200 °C, the S' phase underwent rapid coarsening, which reduced the concentration of Cu and Mg atoms in the matrix. This diminishes the driving force for S' phase nucleation, leading to a significantly lower quantity of S' phase precipitates compared to the sample aged at 180 °C for 2 h.

This phenomenon can also be explained by the results of molecular dynamics (MD) simulations. As shown in Fig. 10(a), the dislocation density decreases with increasing the aging temperature.

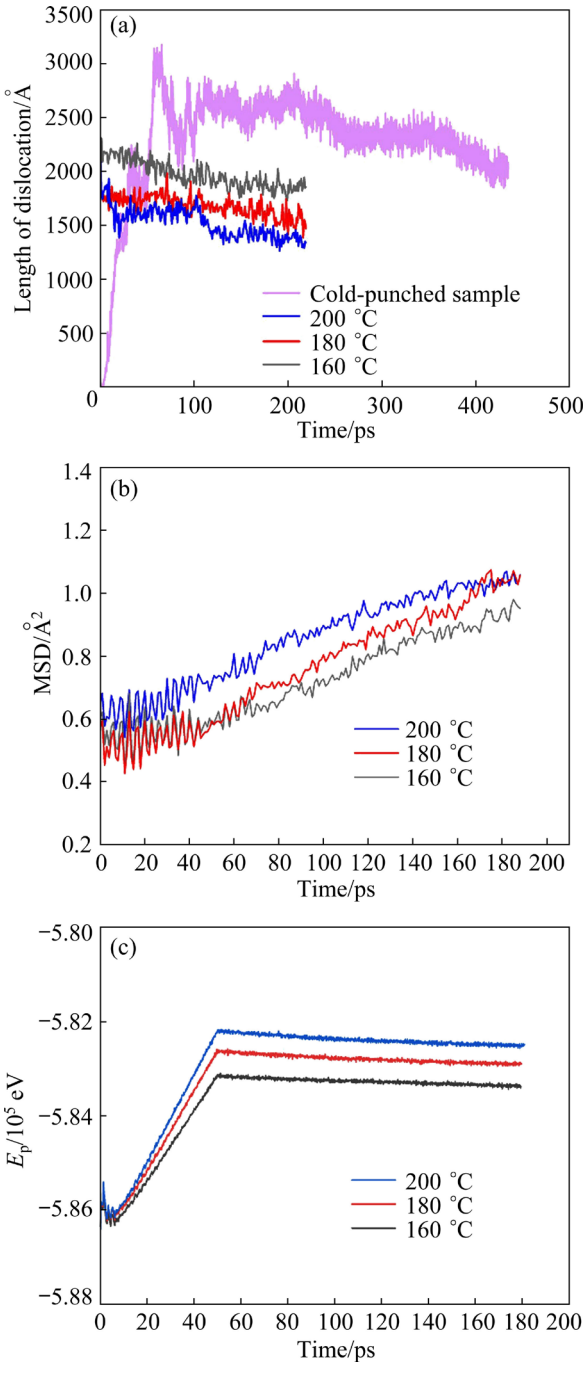

Fig. 10 Length of dislocation (a), mean square displacement (MSD) (b) and potential energy (E_p) (c) of sample at different aging temperatures

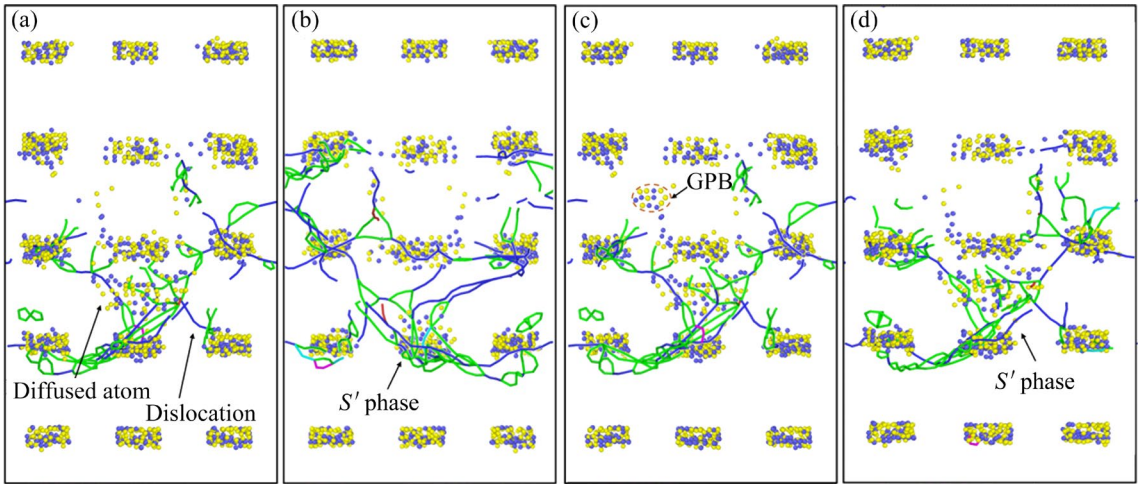

Fig. 11 Snapshot of MD simulations at different aging temperatures: (a) Rapid cold-punched sample; (b) 200 ℃; (c) 180 ℃; (d) 160 ℃

Dislocations, which are crystal defects, serve as rapid diffusion channels for atoms and act as nucleation sites for precipitate phases. When the aging temperature is 160 ℃, the reduction in dislocation length is smaller, indicating a higher number of nucleation sites. In contrast, more significant reductions in dislocation density occur at 180 and 200 °C, resulting in fewer nucleation sites for precipitate phases. Atoms tend to concentrate in regions with high dislocation density, and variations in dislocation density also influence the atomic diffusion rate. From Fig. 10(b), it can be observed that atoms diffuse faster at 180 and 200 °C during the early stages of aging. However, atomic diffusion stabilizes at 180 and 200 °C, while at 160 °C, atomic diffusion continues to accelerate. This difference in diffusion rates leads to variations in the precipitation sequence of the S' phase at different temperatures. The potential energy of the sample at 160 °C is higher than that at the other temperatures, as shown in Fig. 10(c). A high potential energy indicates that the atoms are far from their equilibrium positions. This deviation in atomic positions increases the lattice distortion energy, which further influences the precipitation sequence.

Figure 11 presents snapshots of the cold punching process and aging at different temperatures. During cold punching, the redissolution of the S' phase is induced by severe deformation. At an aging temperature of 200 °C, the precipitation sequence follows SSS→GPB zones→GPB zones + S' → S', attributed to the longer diffusion distances and lower distortion energy at high temperatures. At 180 °C, the reduced diffusion capacity causes atoms to travel shorter distances, resulting in the delayed formation of agglomerated GPB regions (Fig. 11(b)). At 160 °C, where atomic diffusion is minimal, the redissolved atoms fail to reach the dislocations and instead coalesce to form the S' phase.

5 Conclusions

(1) Rapid cold punching followed by the optimal aging treatments significantly enhances the mechanical properties of Al−Cu−Mg alloys. Specifically, aging at 180 °C for 2 h achieves the highest hardness of HV 193 due to the effective precipitation of the S' phase.

(2) The precipitation sequence and phase stability are highly sensitive to aging temperature. At elevated temperatures (e.g., 200 °C), the conventional sequence involving GPB zones is observed, whereas lower temperatures suppress the formation of GPB zones and directly promote S' phase precipitation.

(3) Molecular dynamics simulations reveal that aging temperature governs both atomic diffusion rates and dislocation evolution, directly influencing the nucleation and growth of the S' phase. Higher temperatures accelerate diffusion and promote coarsening, resulting in a trade-off between peak hardness and aging duration.

CRediT authorship contribution statement

Ze-yi HU: Investigation, Methodology, Writing − Original draft, Review & editing; **Pu-yu LI:** Supervision, Writing − Review & editing; **Cai-he FAN** and **Shuai WU:** Investigation, Conceptualization, Funding acquisition, Supervision, Writing − Review & editing; **Yi-ling LU**, **Yin-chun XIAO**, and **Ling OU:** Supervision, Writing − Review & editing.

Declaration of competing interest

The authors declare that they have no known competing financial interests or personal relationships that could have appeared to influence the work reported in this paper.

Acknowledgments

This work was supported by the China Scholarship Council (CSC) Local Cooperation Program (No. 202308430176), the National Natural Science Foundation of China (No. 52271177), and the Hunan Provincial Natural Science Foundation Regional Joint Fund, China (No. 2023JJ50173).

References

[1] HIRSCH J, SKROTZKI B, GOTTSTEIN G. Aluminum alloys: Their physical and mechanical properties [M]. Germany: Elsevier, 2008.

[2] SUI Y L. Aluminum alloys and their forming technology [M]. Beijing: Metallurgical Industry Press, 2020. (in Chinese)

[3] YU Tao, LI Feng, WANG Ye, LI Xue-wen. New powder metallurgy preparation method of homogeneous and isomeric Al−Cu−Mg mixed crystal materials [J]. Transactions of Nonferrous Metals Society of China, 2023, 33(2): 371−382.

[4] GLAZOFF M V, KHVAN A J, ZOLOTOREVSKIĬ V S, BELOV N A, DINSDALE A G. Casting aluminum alloys: Their physical and mechanical metallurgy [M]. 2nd ed. London: Elsevier, 2018.

[5] SONG Yu-feng, ZHANG Qin, DU Wei, DING Xue-feng, CHEN Yu-qiang, LIU Wen-hui. Effect of thermal-cold cycling treatment on microstructural stability of Al−Cu−Mg alloy hemispherical component [J]. Journal of Alloys and Compounds, 2023, 969: 172388.

[6] ZHENG Rui-xiao, SUN Yan-bo, AMEYAMA K, MA Chao-li. Optimizing the strength and ductility of spark plasma sintered Al 2024 alloy by conventional thermo-mechanical treatment [J]. Materials Science and Engineering A, 2007, 55: 5822−5832.

[7] LAOUAR B, HAMANA D, HAYOUNE A. Effect of thermomechanical treatment on the hardening of Al6060 alloy [J]. Materials Science and Technology, 2022, 39: 519−530.

[8] FAN Cai-he, OU Ling, HU Ze-yi, YANG Jian-jun, CHEN Xi-hong. Re-dissolution and re-precipitation behavior of nano-precipitated phase in Al−Cu−Mg alloy subjected to rapid cold stamping [J]. Transactions of Nonferrous Metals Society of China, 2019, 29(12): 2455−2462.

[9] LI Guang-jing, PAN Xing-hui, LIAO Heng-cheng, ZHENG Ji-wei, YANG Mo-tong, QIAN Long-jie, LU Li-zhen. Sn-induced phase transformation mechanism from θ' to θ in Al−4Cu alloy and its influence on high temperature strength [J]. Transactions of Nonferrous Metals Society of China, 2023, 33(9): 2559−2573.

[10] ZHANG Lin-yan, LUO Hong-yun, JIANG Yu-hao. Precipitation kinetics of precipitates with different orientations and segregation in an ultrafine grained Al−Cu−Mg alloy [J]. Journal of Materials Research and Technology, 2024, 28: 1713−1724.

[11] WANG Kai, ZHAN Li-hua, YANG You-liang, MA Zi-yao, LI Xi-cai, LIU Jian. Constitutive modeling and springback prediction of stress relaxation age forming of pre-deformed 2219 aluminum alloy [J]. Transactions of Nonferrous Metals Society of China, 2019, 29(6): 1152−1160.

[12] IRMER D, MOUSSA C, BELKACEMI L, SENNOUR M, VAISSIERE A, ESIN V. Effect of cold rolling on nucleation, growth and coarsening of *S*-phase precipitates in Al−Cu−Mg alloy alloy (AA2024): From heterogeneous nucleation to homogeneous spatial distribution [J]. Journal of Alloys and Compounds, 2023, 963: 171162.

[13] HUANG Wen-jie, LIU Zhi-yi, XIA Lin-yan, XIA Peng, ZENG Su-min. Severe plastic deformation-induced dissolution of θ'' particles in Al−Cu binary alloy and subsequent nature aging behavior [J]. Materials Science and Engineering A, 2012, 546: 26−33.

[14] LI Hai, XU Wei, WANG Zhi-xiu, FANG Bi-jun, SONG Ren-guo, ZHENG Zi-qiao. Effects of re-ageing treatment on microstructure and tensile properties of solution treated and cold-rolled Al−Cu−Mg alloys [J]. Materials Science and Engineering A, 2016, 650: 254−263.

[15] ZHANG Zi-zhao, XU Xiao-chang, LIU Zhi-yi, WU Chun. Effect of strain rate on redissolution rate of precipitated phase at low temperature in severely plastically deformed Al−Cu alloy [J]. Heat Treatment, 2010, 25(2): 15−18. (in Chinese)

[16] HU Ze-yi, FAN Cai-he, SHEN Tong, OU Ling, DAI Nan-shan, WANG Lu. Effect of aging treatment on the evolution of S' phase in rapid cold punched Al−Cu−Mg alloy [J]. Transactions of Nonferrous Metals Society of China, 2021, 31(7): 1930−1938.

[17] SUN Lu, CHEN Liang, GUO Yun-yue, ZHAO Guo-qun. Experimental study and optimization on solution and artificial aging of cold-rolled 2024 Al alloy sheet [J]. Journal of Materials Engineering and Performance, 2022, 31: 5419−5431.

[18] IVAN Z, RUSTAM K. Ageing response of cold-rolled Al−Cu−Mg alloy [J]. Materials Science and Engineering A, 2020, 781: 139148.

[19] LI Hui-zhong, LIU Ruo-mei, LIANG Xiao-peng, DENG Min, LIAO Hui-juan, HUANG Lan. Effect of pre-deformation on microstructures and mechanical properties of high purity Al–Cu–Mg alloy [J]. Transactions of Nonferrous Metals Society of China, 2016, 26(6):

1482−1490.
[20] MASUDA T, SAUVAGE X, HIROSAWA S, HORITA Z. Achieving highly strengthened Al−Cu−Mg alloy by grain refinement and grain boundary segregation [J]. Materials Science and Engineering A, 2020, 793: 139668.
[21] ESIN V, BRIEZ L, SENNOUR L, KOSTER A, GRATIOT A, CREPIN J. Precipitation hardness map for Al−Cu−Mg alloy (AA2024-T3) [J]. Journal of Alloys and Compounds, 2021, 854: 157−164.
[22] FENG Zong-qiang, YANG Yan-qing, HUANG Bin, HAN Ming, LUO Xian, RU Ji-gang. Precipitation process along dislocations in Al−Cu−Mg alloy during artificial aging [J]. Materials Science and Engineering A, 2010, 528: 706−714.
[23] LIU Guo-tan, GAO Wei-hong, HUANG Guo-sheng, SUN Ke-qiang, SUN Bin, FU Jin-lai, LI Ting, CONG Fu-guan, FU Yu-dong. Study on the microscopic mechanism of age-strengthened high damage tolerance Al−Cu−Mg alloys [J]. Vacuum, 2023, 216: 112442.
[24] WANG Jia-qi, SHIN S, NOBAKHT A Y, SHYAM A. Structural deformation and transformation of θ'-Al_2Cu precipitate in Al matrix via interfacial diffusion [J]. Computational Materials Science, 2018, 156: 111−120.
[25] GENG Ji-wei, LI Yu-gang, LIU Gen, XIAO Hong-yu, HONG Tian-ran, HUANG Jie, WANG Ming-liang, CHEN Dong, WANG Hao-wei. Segregation of *S* precipitates at *T*/Al interfaces and relevant effects on localized corrosion mechanisms in Al−Cu−Mg alloy [J]. Materials Characterization, 2012, 31(4): 301−307.
[26] LIU Fei, LIU Zhi-yi, JIA Peng-xiang. Effect of *T*-phase on microstructure of the hot rolled Al−Cu−Mg alloy [J]. Journal of Alloys and Compounds, 2020, 825: 154−158.
[27] CHEN Zhi-guo, ZHANG Ji-shuai, SHU Jun, SHA Gang, XIA Jun-hai, WANG Shi-yong. Effects of Si addition on the microstructure evolution of Al−Cu−Mg alloys in the α+*S*+*T* phase field [J]. Philosophical Magazine Letters, 2013, 93(11): 648−654.
[28] KOVARIK L, MILLS M J. Structural relationship between one-dimensional crystals of Guinier−Preston−Bagaryatsky zones in Al−Cu−Mg alloys [J]. Scripta Materialia, 2011, 64(11): 999−1002.
[29] XU Xiao-chang. Basic investigation on the phenomenon of severe plastic deformation induced re-dissolution of precipitated phases at low temperature and its application [D]. Changsha: Central South University, 2008: 102−105. (in Chinese)
[30] LI L B, SUN Y F. Handbook of physical properties of metallic materials [M]. Beijing: China Machine Press, 2011. (in Chinese)
[31] CURRAN D R, SEAMAN L, SHOCKEY D A. Dynamic failure of solids [J]. Physics Reports, 1987, 147(5): 253−388.
[32] PEI Xiao-yang, PENG Hui, HE Hong-liang, LI Pin. Discussion on the physical meaning of free surface velocity curve in ductile spallation [J]. Acta Physica Sinica, 2015, 64(3): 412−419. (in Chinese)

快速冷冲 Al−Cu−Mg 合金中 *S′* 相的析出行为

胡泽艺[1,2]，李普宇[1]，范才河[1]，武 帅[1]，卢益玲[2]，肖银春[1]，欧 玲[1]

1. 湖南工业大学 材料与先进制造学院，株洲 412007；
2. College of Science and Engineering, University of Derby, Derby, DE22 3BB, UK

摘　要：采用透射电镜(TEM)、高角度环形暗场扫描透射电镜(HAADF−STEM)和分子动力学(MD)模拟等手段，研究了快速冷冲 Al−Cu−Mg 合金中 *S′* 相回溶后形成的过饱和固溶体在不同时效阶段的析出行为。研究结果表明，析出序列与时效温度密切相关，当时效温度能够消除基体晶格畸变时，析出序列与常规序列相同；当时效温度不足以消除基体晶格畸变时，析出序列发生改变，GPB 区的形成受到抑制。分子动力学模拟表明，溶质原子在不同时效温度下的扩散速率差异导致了 *S′* 相析出顺序的变化。

关键词：Al−Cu−Mg 合金；时效处理；*S′* 相演变；快速冷冲；分子动力学模拟

(Edited by Bing YANG)